Sensors & Actuators: B. Chemical 423 (2025) 136762

Contents lists available at ScienceDirect

Sensors and Actuators: B. Chemical

journal homepage: www.elsevier.com/locate/snb

Label-free and sensitive detection of *Citrus Bark Cracking Viroid* in hop using $Ti_3C_2T_x$ MXene-modified genosensor

Alnilan Lobato [a,b], Ivan Konjević [a,c], Sebastjan Radišek [d], Jernej Jakše [e], Helena Volk [e], Monika Hermanová [f], Miroslav Fojta [f], Jan Paštika [g], Zdeněk Sofer [g], Rui Gusmão [g,**], Samo B. Hočevar [a], Nikola Tasić [a,*]

[a] Department of Analytical Chemistry, National Institute of Chemistry, Ljubljana, Slovenia
[b] International Postgraduate School Jožef Stefan, Ljubljana, Slovenia
[c] Faculty of Chemistry and Chemical Technology, University of Ljubljana, Ljubljana, Slovenia
[d] Slovenian Institute of Hop Research and Brewing, Žalec, Slovenia
[e] Biotechnical Faculty, University of Ljubljana, Ljubljana, Slovenia
[f] Institute of Biophysics, Academy of Science of the Czech Republic, Brno, Czech Republic
[g] Department of Inorganic Chemistry, University of Chemistry and Technology Prague, Czech Republic

ARTICLE INFO

Keywords:
CBCVd
Viroid
Hop
RNA detection
Impedimetric genosensor
MXene

ABSTRACT

Since the discovery of *Citrus bark cracking viroid* (CBCVd) in hops in 2007, affected hop-growing countries such as Slovenia and Germany have been actively pursuing efficient and easily accessible diagnostic tools that could contribute to the early detection of CBCVd in the field. In the early stages of CBCVd infection, typical symptoms or subtle signs of spread may not be evident. Detection becomes feasible only when the plant begins to display symptoms. Unfortunately, there is currently no treatment available, which requires the removal of infected plants as the only viable solution. However, this approach leads to significant economic losses on a large scale. This work demonstrates the development and study of a sensitive, selective, and label-free impedimetric genosensor for the detection of CBCVd in total RNA hop samples. The genosensor is based on a supporting glassy carbon electrode modified with streptavidin-agarose beads, which serve as an effective immobilization layer for a biotinylated single-stranded DNA capture probe. The integration of a 2D-layered $Ti_3C_2T_x$ MXene into the sensing architecture resulted in a significantly improved electroanalytical performance of the genosensor. Several fabrication and operational parameters were optimized, such as the streptavidin-agarose beads deposition time, capture probe immobilization time and concentration, and sample incubation time. The optimized genosensor exhibited a limit of detection of only 0.5 fg μL^{-1} (5.5 fmol L^{-1}) in combination with a one-hour incubation with the denatured total RNA hop extract, thus eliminating the need for an additional and laborious amplification step.

1. Introduction

The hop (*Humulus lupulus L.*) is an economically important crop due to the worldwide use of its secondary metabolites in breweries [1] and pharmaceutical companies [2]. Over the past three decades, global hop production has surged, with the United States and Germany leading the way [3]. Hops are susceptible to many diseases, including those caused by viroids, the smallest biological pathogens capable of replication using host enzymes. Viroid infections can be highly aggressive, resulting in reduced plant growth, dwarfing, abnormal leaf shapes, yellowing, necrosis, and leaf rolling [4]. The structure of viroids consists of non-encapsulated, single-stranded, circular RNA molecules ranging in size from 239 to 401 nucleotides, whose nucleotide sequence does not allow protein-coding [5]. Viroids spread through various ways,

* Corresponding author at: Department of Analytical Chemistry, National Institute of Chemistry, Ljubljana, Slovenia.
** Corresponding author at: Department of Inorganic Chemistry, University of Chemistry and Technology Prague, Czech Republic.
E-mail addresses: alnilan.lobato@ki.si (A. Lobato), ivan.konjevic@ki.si (I. Konjević), sebastjan.radisek@ihps.si (S. Radišek), Jernej.Jakse@bf.uni-lj.si (J. Jakše), Helena.Volk@bf.uni-lj.si (H. Volk), hermanova@ipb.cz (M. Hermanová), fojta@ibp.cz (M. Fojta), jan.pastika@vscht.cz (J. Paštika), zdenek.sofer@vscht.cz (Z. Sofer), rui.gusmao@vscht.cz (R. Gusmão), samo.hocevar@ki.si (S.B. Hočevar), nikola.tasic@ki.si (N. Tasić).

https://doi.org/10.1016/j.snb.2024.136762
Received 26 April 2024; Received in revised form 7 October 2024; Accepted 9 October 2024
Available online 11 October 2024

predominantly by mechanical contact with agricultural equipment, by leaf-to-leaf contact, and by human handling, as well as by seeds, pollen, and insect vectors [6].

The *Citrus bark cracking viroid* (CBCVd) was first discovered in citrus fruits in 1988 and was classified as a mild pathogen for these plants [7, 8]. However, in 2007, CBCVd was discovered in Slovenian hop plants, leading to the complete eradication of over 300 ha of hop fields due to the viroid's aggressive nature [9,10]. CBCVd is particularly devastating for hop cultivation, causing severe symptoms such as plant stunting (reduced growth and overall size compared to healthy plants), root dry rot, and plant dieback three to five years after infection. Despite the Slovenian national eradication program, CBCVd continues to threaten farmers and hop production as an emerging highly aggressive pathogen. In 2019, a CBCVd outbreak appeared in Germany, and the most recent report comes from Brazil in 2023 [11], posing a threat to hop-growing regions in Europe and worldwide [10].

The emergence of such pathogens underlines the urgent need for rapid and straightforward viroid detection methods. Early identification of plant diseases can prevent or limit the spread of emerging infections, ultimately reducing costs and minimizing damage caused by contamination [12]. The insidious nature of CBCVd, characterized by the absence of typical symptoms or the presence of only atypical symptoms during the early stages of infection, highlights the importance of simple and reliable on-site detection for farmers [9].

Typically, the identification of pathogens such as viruses and viroids relies on conventional or advanced molecular biology techniques [13]. These methods tend to be both costly and time-consuming. Examples of such methods include polymerase chain reaction (PCR), reverse transcription quantitative PCR (RT-qPCR), loop-mediated isothermal amplification (LAMP), enzyme-linked immunosorbent assay (ELISA), and CRISPR-Cas-based detection [14].

Alternatively, electrochemistry offers simple and cost-effective approaches for detecting microbial pathogens. Designing biosensors for plant pathogens typically involves the modification of the electrode surface to immobilize biological recognition elements for interaction with the target [15]. While significant progress has been made in the development of electrochemical biosensors for plant pathogens over the past three decades [16], reports specifically addressing viroids remain scarce. For example, a graphene/zinc oxide nanocomposite genosensing platform capable of detecting a CCCVd (*Coconut cadang-cadang viroid*) RNA oligonucleotide over a linear range of 1.0×10^{-11} M to 1.0×10^{-6} M was presented [17]. The initial modification layer was functionalized with 1-pyrenebutyric acid N-hydroxysuccinimide ester to enable chemical binding of the single-stranded DNA capture probe. Subsequent hybridization with the single-stranded RNA oligonucleotide target was monitored by either electrochemical impedance spectroscopy (EIS) or differential pulse voltammetry (DPV). More recently, a similar genosensor for CCCVd detection was developed based on gold nanoparticles decorated phosphorene nanohybrid with graphene, which achieved a similar linear range of 1.0×10^{-11} M to 1.0×10^{-6} M, with a limit of detection of 2.8×10^{-12} M [18]. In both studies, the detection target consisted of artificially prepared single-stranded RNA corresponding to a segment of the CCCVd sequence.

In this work, a sensitive and selective genosensor was demonstrated, exploiting streptavidin-agarose beads as a biocompatible immobilization matrix for a single-stranded DNA capture probe and the attractive electrocatalytic properties of 2D-layered $Ti_3C_2T_x$ MXene. The genosensor successfully detected CBCVd in infected total RNA hop samples obtained directly from the field, without the need for labeling or laborious amplification steps.

2. Experimental

2.1. Chemicals and materials

All reagents were of analytical grade and were used without further purification. All aqueous solutions were prepared using ultrapure water with resistivity not less than 18.2 MΩ cm at 298 K (Milli-Q, Millipore, Corp., Marlborough, USA). Titanium aluminum carbide (Ti_3AlC_2) was acquired from Jinzhou Haixin Metal Materials (China).

Streptavidin-agarose beads (STR-AGAR beads) from *Streptomyces avidinii*, sodium hydroxide (NaOH), and sodium chloride (NaCl) were purchased from Merck (Darmstadt, Germany), sodium azide (NaN_3), glycine, and bovine serum albumin (BSA) from Sigma Aldrich (St. Louis, USA), disodium hydrogen phosphate dihydrate ($Na_2HPO_4{\cdot}2\ H_2O$) from Kemika (Zagreb, Croatia), alumina (Al_2O_3, 0.3 μm) and polishing cloth from Buehler (Lake Bluff, USA), potassium dihydrogen phosphate (KH_2PO_4) and potassium hexacyanoferrate (III) ($K_3[Fe(CN)_6]$) from Fluka (Switzerland), and potassium chloride (KCl) and potassium hexacyanoferrate (II) ($K_4[Fe(CN)_6]$) from Riedel-de Haën (Seelze, Germany). TE buffer (10 mM Tris-HCl, 1 mM EDTA, pH 8.0) and nuclease-free water were purchased from Integrated DNA Technologies (Coralville, USA). The phosphate-buffered saline (PBS, pH=7.4) consisted of 8.00 g of NaCl, 200.0 mg of KCl, 1.81 g of $Na_2HPO_4{\cdot}2\ H_2O$, and 240.0 mg of KH_2PO_4 in 1.0 L purified H_2O.

The capture probe sequence, 50 bp in length (5′-AGAGTTGTATCCACCGGGTAGTTTCTTTCTCAGGTCGCGAAGGAAGAAGC-3′), was synthesized by Eurofins Genomics (Germany) with a biotin moiety attached to the 5′ end. This probe was designed based on the sequence of the CBCVd isolate Hl-1 (GenBank accession number KM211546.1). The capture probe anneals perfectly to the region spanning nucleotides 182–231 of the CBCVd genome.

2.2. Total RNA isolation and CBCVd quantification

The viroid source was infected hop plants of the variety 'Celeia' from the pathogen reference collection of the Diagnostic Laboratory for Plant Protection at the Institute of Hop Research and Brewing, Žalec, Slovenia. The plants were biolistically inoculated in 2013 with infectious cDNA constructs (GenBank X07397, GenBank KM211546, GenBank X07405) of single viroids (CBCVd, HLVd) and combinations (CBCVd+HLVd and HSVd+HLVd) [19]. Viroid-free hop plants of the same variety and tomato (*Solanum lycopersicum L.*; cv. Heinz 1370) plants served as the source of negative control plant samples. From each plant, three fully developed leaves were sampled at phenological stage BBCH 38 for hops and BBCH 29 for tomatoes, then stored at −80°C until being used for RNA isolation. Total RNA was extracted from 100 mg of leaf tissue taken from all three sampled leaves of each plant using a CTAB protocol without DNase treatment [20]. The total RNA was eluted in 50 μL of a TE buffer (10 mM Tris-HCl, 1 mM EDTA, pH 8.0). The RNA concentration was measured using the Qubit® 3.0 Fluorometer (Thermo Fisher Scientific, USA) and stored at −80°C (Table S1).

The High-Capacity cDNA Reverse Transcription Kit (Thermo Fisher Scientific, USA) was used to produce cDNA from total RNA hop samples containing 500 ng RNA. The absolute quantification of CBCVd was performed by 7500 Real-Time PCR System (Thermo Fisher Scientific, USA) using a linearised plasmid containing CBCVd sequence as standards. The reaction was performed using SybrGreen chemistry and primers CBCVd-PCR-F-q: 5'-TCACTGGCGTCCAGCACC-3' and CBCVd-PCR-R-q: 5'-AGGAAGAAGCGACGATCGG-3' [21].

2.3. Synthesis of $Ti_3C_2T_x$ MXene

The synthesis of $Ti_3C_2T_x$ MXene followed the same protocol as previously published [22]. Briefly, the precursor Ti_3AlC_2 MAX phase was etched with 40 % HF for four days, followed by LiF/HCl for two days. The product was then repeatedly washed and centrifuged with H_2O until approaching neutral pH, being dried at 50°C in a vacuum oven. The resulting material was then stored in polar organic solvent at 4ºC.

2.4. Characterization of $Ti_3C_2T_x$ MXene

The morphology of the precursor and synthesized materials was examined by scanning electron microscopy (SEM) with field emission Tescan LYRA$_3$ GM dual-beam microscope and Tescan MAIA$_3$ (Tescan, Czech Republic) at an acceleration voltage of 5 kV. Elemental composition was investigated by energy-dispersive X-ray spectroscopy (EDX) using an X-MaxN detector from Oxford Instruments at 20 kV acceleration voltage. For both SEM and EDX analyses, the Ti_3AlC_2 powder and the colloidal suspension of $Ti_3C_2T_x$ MXene were drop-cast on copper tape. Scanning transmission electron microscopy (STEM) was performed at Tescan MAIA$_3$ electronic microscope with a STEM sample holder and X-MaxN 150 EDX detector. The diluted suspension of MXene was drop-cast on a 200 mesh Cu TEM grid (Ted Pella, USA), and then dried. STEM measurements were carried out using a 30 kV electron beam. An InVia Raman microscope (Renishaw, England) was used for Raman spectroscopy measurements in backscattering geometry with a CCD detector. An Nd:YAG laser (532 nm, 50 mW) with a 2400 line mm^{-1} diffraction grating, an applied power of 5 %, and a 20x objective were used for the measurements. The Raman spectrum was collected with 100 accumulations in the Raman range of 100–900 cm^{-1} at room temperature. X-ray diffraction (XRD) measurements were carried out using a Bruker D2 Phaser benchtop diffractometer (Bruker, Germany) with a Cu Kα radiation source (λ=1.54178 Å). The diffraction patterns were acquired in the range of 2θ from 5 to 80° at room temperature. The data were evaluated by HighScore Plus 4.9 software. Fourier transform-infrared spectroscopy (FTIR) measurements were performed on a Nicolet iS50R FTIR spectrometer (Thermo Scientific, USA). The measurement was performed with a DLaTGS detector and a KBr beam splitter in the range 4000–400 cm^{-1} at a resolution of 4 cm^{-1}, with a total of 265 scans. FTIR spectra were measured in a KBr pellet made from 300 mg of KBr and 1 mg of materials. OMNIC software was used to acquire and process the data. Baseline correction and data treatment were performed according to recommendations by T. Parker et al. [23].

2.5. Genosensor fabrication

Before use, the GCE underwent mechanical polishing using 0.3 μm alumina slurry. The GCE was then sonicated in ethanol for 2 min, washed with ultrapure water, and dried using high-purity nitrogen gas (0.2 bar). Next, 40 mg of commercial STR-AGAR beads were dissolved in 2 mL of phosphate-buffered saline (PBS, pH 7.4) containing 0.03 % sodium azide. 10 μL of the STR-AGAR beads solution was carefully drop-casted onto the GCE surface and stored at 4 °C for 2 h.

Modification with $Ti_3C_2T_x$ MXene: the electrocatalytic 2D-layered $Ti_3C_2T_x$ MXene in ethanol was heated to approximately 30°C until the solvent evaporated slowly. The remaining powder was then redispersed in ultrapure water to obtain an aqueous solution with a concentration of 2 mg mL^{-1}. After vortexing for 1 min, the MXene suspension was mixed with the STR-AGAR beads solution in a 1:1 ratio. The resulting $Ti_3C_2T_x$-STR-AGAR mixture was vortexed for 10 seconds before depositing 4.5 μL of it onto the supporting GCE surface and stored at 4 °C for 2 h.

Between each modification step, the electrode surface was rinsed with ultrapure water for 1 min and dried using a gentle stream of nitrogen gas (0.2 bar).

Next, 8 μL of the biotinylated capture probe solution (50 ng μL^{-1}) was drop-casted onto the modified electrode surface and incubated for 2 h at 4 °C. To prevent non-specific binding, 8 μL of glycine solution (10 μg mL^{-1}) was deposited onto the surface of the genosensor for 30 min at 4 °C.

2.6. EIS genosensing

Total RNA hop samples extracted from hop plants underwent denaturation in a 95°C water bath for 3 min, followed by rapid cooling on ice for 1 min. Finally, 8 μL of the real sample solution was applied to the sensor surface and incubated for 60 min at room temperature. The sensor was then quickly rinsed with ultrapure water, and electrochemical detection was conducted in the presence of 5 mM $[Fe(CN)_6]^{3-/4-}$ in 0.1 M KCl. The fabrication of the genosensor and detection of CBCVd are depicted in Fig. 1.

2.7. Electrochemical measurements

Cyclic voltammetric (CV) and electrochemical impedance spectroscopic (EIS) measurements were carried out with a portable PalmSens 4 electrochemical workstation (potentiostat/galvanostat) operated by the PSTrace 5.9 software (PalmSens BV, Netherlands). In all experiments, a glassy carbon supporting electrode (GCE, 3 mm) was used, in combination with a single junction Ag/AgCl/KCl(satd.) reference electrode, and a Pt rod as the counter electrode. All electrodes were purchased from Metrohm (Herisau, Switzerland). EIS spectra were recorded in the frequency range of 10^5-10^{-1} Hz, at the potential of +0.14 V, with an amplitude of 5 mV, in a solution of 5 mM $[Fe(CN)_6]^{3-/4-}$ in 0.1 M KCl. CV measurements were performed in the potential range of −0.5–1.0 V or −0.2–0.6 V, with a scan rate of 100 mV s^{-1}.

3. Results and discussion

3.1. Optimization of the genosensor fabrication and operation

The genosensor development protocol was optimized with respect to several parameters. The increase in charge transfer resistance (R_{ct}) of the genosensor before and after incubation with a total RNA hop sample infected with CBCVd was used as a feedback signal to determine the optimal fabrication and measurement parameters, i.e., $\Delta R = R_{inc}$-R_{blank}. All R_{ct} values, i.e., R_{inc} (after sample incubation) and R_{blank} (before sample incubation), were determined by fitting the raw impedance spectra with a Randles-type equivalent electrical circuit ($R_S([R_{ct}Z_W]Q_{dl})$) representing the real physicochemical processes at the genosensor/electrolyte interface. Herein, R_S corresponds to the solution resistance, Q_{dl} is the constant phase element (CPE) accounting for the non-ideal double-layer capacitance, R_{ct} is the charge transfer resistance of the genosensor/electrolyte interface, and Z_W is the Warburg element that models the diffusion phenomenon. Firstly, we optimized several key parameters influencing the performances of the CBCVd genosensor, i.e., (i) STR-AGAR beads deposition time, (ii) capture probe immobilization time, (iii) sample incubation time, and (iv) capture probe concentration.

The interaction between streptavidin, a tetrameric protein from *Streptomyces avidinii*, and biotin, a water-soluble vitamin, is one of the fundamental and widespread phenomena in molecular biology and biotechnology [24,25]. This interaction has found numerous applications, including affinity purification [26], immunoassays [27], and biosensing [28]. In addition to a strong immobilization of the biotinylated single-stranded DNA capture probe, the STR-AGAR beads serve as an effective adhesion agent to prevent leaching of the sensing layer from the electrode surface and its dissolution during exposures to solutions in the subsequent fabrication steps. The STR-AGAR beads were introduced from the 20 mg mL^{-1} PBS solution (pH 7.4) by a simple drop-casting procedure at 4°C. As depicted in Fig. 2a, the highest analytical signal of the genosensor for 720 fg μL^{-1} CBCVd was obtained when STR-AGAR beads were left to deposit for two hours, whereas shorter and longer deposition times resulted in lower signals. After the optimization of the STR-AGAR beads deposition time, we investigated the effect of the biotinylated capture probe immobilization time upon the genosensor impedimetric response. It was observed (Fig. 2b) that the two-hour immobilization exhibited the highest performance of the genosensor, considering both the signal height and reproducibility when compared to the shorter or longer exposure times to the biotinylated capture probe. The binding event between the STR units confined to the electrode surface and the biotinylated capture probe moieties is a dynamic process that also involves the reverse reaction; however, at the

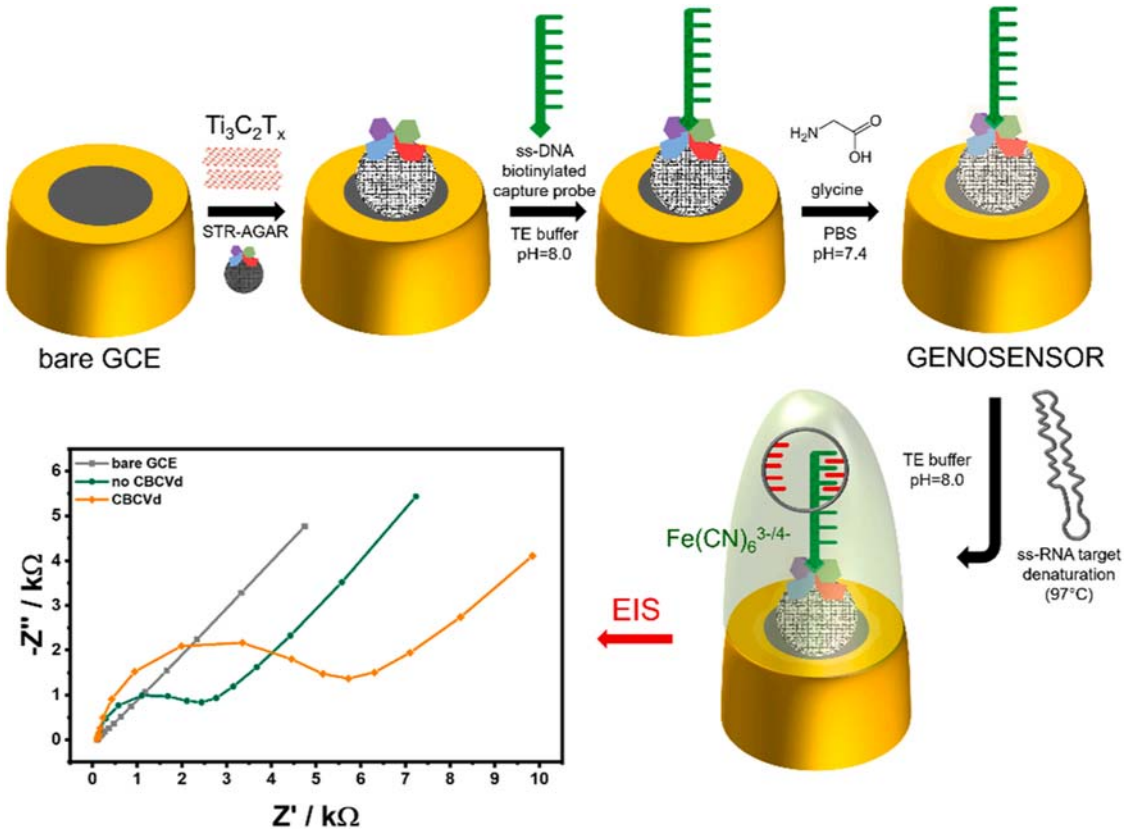

Fig. 1. Fabrication of the CBCVd genosensor and its impedimetric detection.

same time, the steric effects should be taken into consideration [25]. Consequently, a one-hour immobilization might be insufficient to stabilize the sensing surface with the immobilized capture probe; in contrast, longer immobilization times than two hours promote the reverse reaction, i.e., detachment of the capture probe, and/or its improper conformation that leads to poorer performance. Finally, we optimized the time necessary for incubating the total RNA hop sample, and the corresponding results are shown in Fig. 2c. As can be seen, shorter incubation times of 15 and 30 min led to significantly lower signals in comparison with incubation times of 60 and 90 min. Notably, the incubation time of 60 min revealed the highest impedimetric signal along with favorably improved reproducibility. In continuation, all experiments in this study were carried out using the incubation time of one hour.

The next study tackled the effect of capture probe concentration on the genosensor performance, as shown in Fig. S1. Evidently, the impedimetric response was the highest when the biotinylated capture probe concentration was 50 ng μL^{-1}, along with its favorable reproducibility; this concentration was used for all subsequent studies.

3.2. *Electrochemical characterization of the genosensor fabrication*

Using previously optimized parameters, a step-by-step investigation of the genosensor fabrication process was conducted in combination with CV and EIS detection in 5 mM $[Fe(CN)_6]^{3-/4-}$ + 0.1 M KCl, including the final incubation step in total RNA hop samples. By following the electrochemical signals, we gained insights and control into gradual changes occurring at the genosensor surface upon each

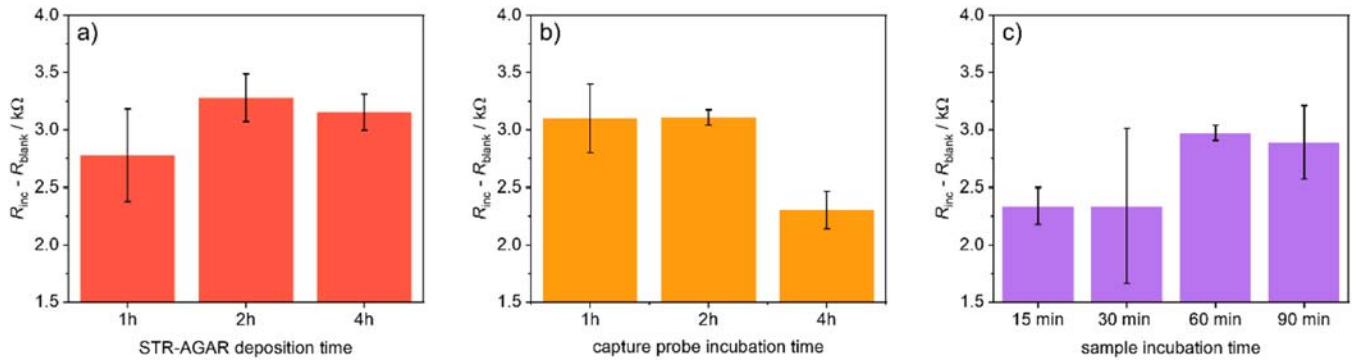

Fig. 2. The effect of (a) STR-AGAR beads deposition time (capture probe incubation time: 2 h, sample incubation time: 60 min), (b) capture probe incubation time (STR-AGAR beads deposition time: 2 h, sample incubation time: 60 min), and (c) sample incubation time (STR-AGAR beads deposition time: 2 h, capture probe incubation time: 2 h) upon the genosensor response. The concentration of CBCVd was 720 fg μL^{-1}, and the concentration of the capture probe was 25 ng μL^{-1}. The error bars represent the relative standard deviation of three independent measurements. Relevant EIS datasets corresponding to the optimization studies are presented in Table S2.

modification step, attaining feedback to successfully fabricate a genosensor with optimized sensitivity and reproducibility. Using a simple Randles circuit $R_S([R_{ct}Z_W]Q_{dl})$, we quantified the impedimetric changes occurring at the genosensor/electrolyte interface. The bare GCE exhibited an impedimetric behavior with a negligible high-frequency semicircle and a diffusion tail typical for conductive carbon surfaces (Fig. 3a). After the introduction of STR-AGAR beads, the impedimetric spectrum altered with the formation of a semicircle, corresponding to a significant increase in the charge-transfer resistance due to the deposition of a less conductive coating. In addition, the incorporation of a biotinylated capture probe further increased the size of the semicircle, reflecting an increased R_{ct}; similarly, the last modification layer, including glycine, contributed to a significantly enlarged R_{ct}, as shown in Fig. 3a. Finally, the dark-green EIS spectrum shows the genosensor response after incubation in a real total RNA hop sample solution of 250 fg μL^{-1} CBCVd, revealing a well-developed impedimetric signal. Similarly, the cyclic voltammograms (Fig. 3b) showed a stepwise decrease of the anodic and cathodic signals of $[Fe(CN)_6]^{3-/4-}$ accompanied by increasing peak-to-peak separation that corresponds to the deposition of genosensor building blocks, reflecting the changes of the interface diffusion pattern. A small signal observed at bare GCE (at ca. −0.4 V) can be attributed to the oxygen reduction reaction. At the same time, Fig. 3 demonstrates a significantly enhanced sensitivity of the EIS vs. CV, particularly considering the detection of the CBCVd viroid in the real sample (dark-green curve).

To test both the potential influence of the supporting buffer and the stability of the sensing layer, 8 μL of the TE buffer was drop-casted onto the fully fabricated genosensor, followed by a one-hour incubation step. As shown in Figure S2, the incubation for one hour in the TE buffer did not affect the EIS response of the genosensor; this was also supported by the fitting parameters, indicating negligible changes, as shown in Table S4.

The incorporation of the Ti_3C_2Tx MXene into the genosensor architecture unveiled a significant improvement in the electrochemical communication between the upper genosensor interface, where hybridization and detection take place, and the lower part, which includes the STR-AGAR beads combined with Ti_3C_2Tx MXene and the supporting GCE. MXenes are state-of-the-art 2D-layered materials composed of transition metal carbides or nitrides, which exhibit remarkable versatility in various application areas, such as catalysis [29,30], ion batteries [31,32], gas sensors [22,33], and biosensors [34,35]. Upon introducing $Ti_3C_2T_x$, MXene, the preliminary measurements revealed a ca. 5-fold increase in the sensitivity of the genosensor for detecting CBCVd in real total RNA hop samples. The step-by-step fabrication of the $Ti_3C_2T_x$ MXene-modified genosensor is shown in Figure S3, with the corresponding fitting parameters listed in Table S5.

3.3. Structural and surface characterization of $Ti_3C_2T_x$ MXene

The MXene $Ti_3C_2T_x$ was obtained by selective etching of the Al layer of the precursor Ti_3AlC_2 MAX phase, as described in the Experimental section. The SEM and STEM micrographs of the observed flakes displayed the typical accordion-like morphology of the multilayer $Ti_3C_2T_x$ MXene, as shown in Fig. 4a and S4. The flakes exhibit tightly packed and loosely packed features depending on the extension in which Al atoms are replaced by surface functional groups such as oxygen (-O), hydroxyl (-OH), or fluorine (-F) [36]. Subsequently, the interlayer forces become weaker, making their delamination possible. The EDX mapping of elements of the detailed area of the selected $Ti_3C_2T_x$ flake with loosely packed sheets is shown in Fig. 4b, which shows the abundant distribution of C, O, F, and Ti elements, while Al is scarcely detected. Another example of SEM/EDX mapping for Ti_3AlC_2 and $Ti_3C_2T_x$ is shown in Figure S4. The averaged EDX spectra of Ti_3AlC_2 and $Ti_3C_2T_x$, obtained on multiple flakes at 20 kV, are shown in Fig. 4c, and the respective quantification in Table S6. In both cases, the quantified at% of Ti/C indicates a ratio of 1.3, close to the expected for Ti_3C_2 stoichiometry of 1.5. One of the major differences between the EDX spectra of the materials is the significant decrease of the Al Kα1 line at 1.4 keV, from an initial 17.3 at% to a considerably lower amount of 1.7 at%, also indicating the successful etching of the precursor Ti_3AlC_2 MAX phase. Furthermore, for $Ti_3C_2T_x$, a new peak is quantified at 0.68 keV corresponding to the F Kα line at a level of 26.8 at% for F. The level of quantified O also increased by 20 % for the $Ti_3C_2T_x$ after the etching of the MAX phase. Both levels of F and O elements are related to the surface functional groups mentioned before.

The Raman spectrum of the precursor MAX phase and MXene obtained in the 100–900 cm^{-1} range, are shown in Fig. 4d, providing information related to the bonds present in the structure by assessing lattice vibrations. For the starting Ti_3AlC_2, the peaks at 148, 244, and 434 cm^{-1} correspond to the $E_{2\,g}$, $E_{1\,g}$, and $A_{1\,g}$ vibrational modes, respectively [37]. The peak at 608 cm^{-1} can be assigned to $E_{1\,g}$ vibration modes corresponding to the in-plane vibration of the Ti–C bond [38]. In comparison, for the $Ti_3C_2T_x$ MXene, with the Al layer etching, surface functional groups (=O, -OH, and –F terminations) are adsorbed and intercalated within the interlayer spacing, causing variations in the local environment of the atoms and affecting lattice vibrations of the unit cell.

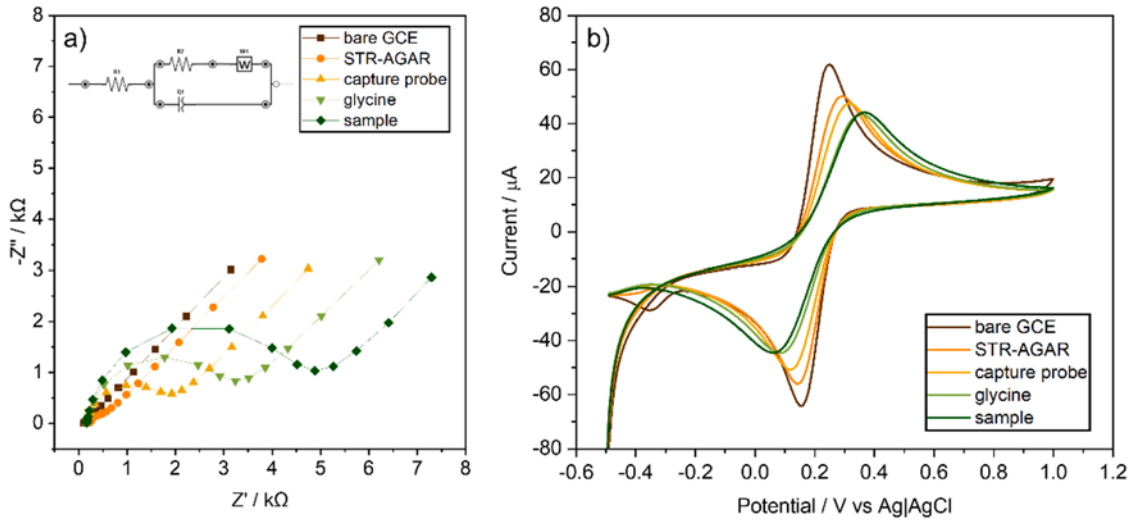

Fig. 3. Characterization of the step-by-step fabrication of the genosensor using (a) EIS and (b) CV measurements in 5 mM $[Fe(CN)_6)]^{3-/4-}$ + 0.1 M KCl. The corresponding fitting parameters are listed in Table S3.

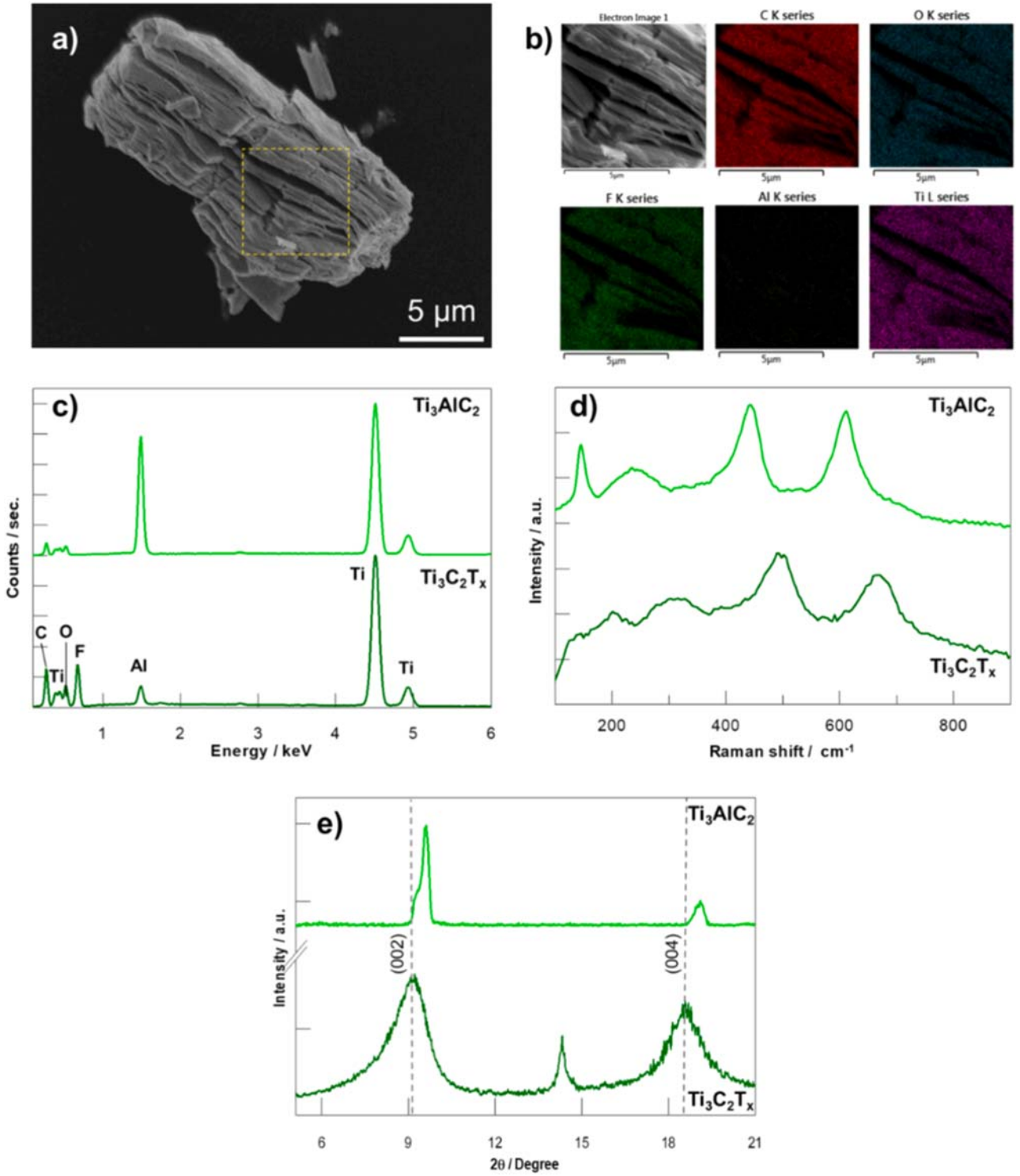

Fig. 4. (a) Overlay of in-beam BSE and SE modes micrograph of a $Ti_3C_2T_x$ MXene multilayer flake after etching with the highlight of the area used for (b) EDX mapping of elements, (c) averaged EDX spectra of Ti_3AlC_2 MAX phase and $Ti_3C_2T_x$ MXene, and (d) comparison of Raman spectrum of Ti_3AlC_2 MAX phase and $Ti_3C_2T_x$ MXene with 532 nm LL. (e) X-ray diffraction (XRD) patterns for low 2θ region with vertical lines marking the position of (002) and (004) peaks of ICDD card no. 04–14–5068.

Thus, the $Ti_3C_2T_x$ spectrum peaks have broadened and a blue shift to higher Raman frequencies. The peak at 148 cm^{-1} was initially intense for Ti_3AlC_2, displaying in-plane vibration Ti atoms, with the major contribution of Ti-Al vibrations, for the case of $Ti_3C_2T_x$ is greatly decreased, broadened, and shifted to 201 cm^{-1}. The remaining peaks of MXene have higher Raman shifts but peak intensities were sustained, with the peak at 314 cm^{-1} having contributions from out-of-plane vibration of the Ti–C bond and H atoms of $Ti_3C_2(OH)_2$ [39]. The peak at 492 cm^{-1} has contributions of in-plane vibration of O atoms of OH MXene terminations [40].

X-ray diffraction (XRD) was used to analyze the crystal structure and phase composition of both materials and further understanding of the successful synthesis of $Ti_3C_2T_x$. As shown in Figure S5a and Fig. 4e, there is a good match of the diffraction pattern of the precursor Ti_3AlC_2 and

the ICDD card no. 04–14–5068 [41], displaying a well-crystallized structure, corresponding to layered ternary 312 MAX phase, with a hexagonal crystal system and $P6_3/mmc$ space group. In Fig. 4e, for the region $5^o<2\theta<21^o$, the MAX phase presents the typical diffraction peaks mainly at $2\theta=9.6^\circ$ and 19.1° for (002) and (004) planes, respectively. There was a shift to lower 2θ values for peaks (002) and (004), 9.1^o and 18.6^o respectively for $Ti_3C_2T_x$. This is caused by the etching procedure in the synthesis of $Ti_3C_2T_x$, removing the Al layers in the initial structure of the MAX phase and induction of new surface terminations in $Ti_3C_2T_x$ (T_x =−F, −O, −OH) [37,42].

As shown in Figure S5b, the FTIR spectrum of the materials exhibits two distinct regions: a 4000–1400 cm^{-1} region dominated by peaks associated with H_2O and C bond vibrations, and a 1400–400 cm^{-1} region characterized by chemical fingerprint peaks, related to C-F, Ti-F, Ti-O, and Ti-C vibrations [23]. For both materials, within the 4000–1400 cm^{-1} region, the presence of adsorbed H_2O is evidenced by the O-H stretching at 3600–3200 cm^{-1}. Additionally, the O-H bending at 1500–1300 cm^{-1} indicates the presence of -OH surface terminations. The C- bond, including C-H stretching, C═O stretching, C-O stretching, and C-H bending, are also observed in this region. For $Ti_3C_2T_x$, in the 1400–400 cm^{-1} region, the C-F stretching within 1400–1000 cm^{-1} is indicative of F surface terminations at defect sites and flake edges, and Ti-C stretching at 464 cm^{-1} was also observed in this region. Within the fingerprint region, the Ti-O bending vibrations are the most intense at 560 cm^{-1}, typically at 650–550 cm^{-1} range. The Ti-F bending, with a typical position of 1000–850 cm^{-1}, is prominent at 856 cm^{-1}. Some shifts seemed to occur due to the simultaneous presence of Ti, O, and F on the surface of $Ti_3C_2T_x$, and the presence of confined H_2O influencing the vibration fingerprint. The C-O stretching exhibits a blue shift from its regular position of 1300–1100 cm^{-1} to the 1622 cm^{-1} range [23]. These results are also consistent with previous XPS analysis of $Ti_3C_2T_x$ [22], in which the Ti 2*p* core level was deconvoluted with Ti $2p_{3/2}$ and Ti $2p_{1/2}$ peaks assigned to the presence of Ti(IV), Ti(III), and Ti(II) oxidation states. The peaks for the Ti(IV) oxidation state were more intense compared to the other oxidation states, implying a relatively higher surface atomic concentration of Ti(IV)-containing species.

The as-prepared $Ti_3C_2T_x$ suspension contains inherent polydispersity of the flakes, with a wide range of lateral sizes, as shown in Figures S4g and S4h, which yields an average of 2.05 μm. The Tyndall scattering effect by irradiation of a green laser beam through the vial of diluted 0.5 mg mL^{-1} MXene dispersion in water is clearly visible, as shown in the inset of Figure S4h. The above results confirm the successful etching of the MAX phase and synthesis of $Ti_3C_2T_x$ that was subsequently used in the genosensor application.

3.4. Analytical performance of the genosensor in real samples

Once the genosensor was fully assembled, further studies were carried out to assess its electroanalytical performance for detecting low concentrations of CBCVd in real samples (Table S1). Notably, we selected the concentration range of CBCVd, mirroring the actual expected concentrations of field-infected plants, by diluting a real total RNA hop sample of a known high concentration of CBCVd.

The performance of the genosensor was investigated by following its impedimetric response when increasing the concentration of CBCVd in a very low concentration range of 0.78–100 fg μL^{-1} (Fig. 5). The genosensor exhibited a highly linear operation in the examined concentration range with an r^2 of 0.99; the calibration curve is characterized by small standard errors for lower CBCVd concentrations and a somewhat large error bar at the highest examined concentration. This can be attributed to the saturation of the sensing surface with the analyte. In contrast, at lower concentrations, the genosensor exhibited higher reproducibility that can be attributed to the mitigated matrix effect due to dilutions of total RNA hop samples, as the real samples utilized in this study exhibited a high degree of CBCVd infection, necessitating their dilutions.

A very low limit of detection (3σ criterium) was achieved, i.e., 0.5 fg μL^{-1} (5.5 fmol L^{-1}) CBCVd. Such electroanalytical characteristics can be considered remarkable performance for a label-free sensing approach, obviating the need for an additional and time-consuming amplification step.

3.5. Reproducibility and selectivity studies

The genosensor showed good intra-day repeatability and satisfactory inter-day reproducibility. For the intra-day repeatability (n = 3), a value of 12 % was obtained at a CBCVd concentration of 6.25 fg μL^{-1}. Regarding inter-day reproducibility (n = 5), a value of 14.9 % was observed at a concentration of 1.56 fg μL^{-1}.

Finally, the selectivity study was conducted by performing EIS measurements with the newly developed genosensor incubated with solutions of (i) total RNA hop sample infected with CBCVd, (ii) viroid-free total RNA hop sample, (iii) viroid-free total RNA tomato sample, and (iv) total RNA hop sample infected with *Hop latent viroid* (HLVd). All samples had total RNA concentration of 5 ng μL^{-1}, while the CBCVd concentration in the CBCVd-infected sample was 6.25 fg μL^{-1}. In addition to a very high sensitivity, the genosensor showed a favorable selectivity, as depicted in Fig. 6.

When testing a non-infected total RNA tomato sample and a total RNA hop sample infected with HLVd, both yielded low signals compared to the CBCVd-infected hop sample with the same total RNA concentration. In contrast, a viroid-free total RNA hop sample exhibited even a negative impedimetric response, which could be due to the undefined matrix effect. Such genosensor characteristics hold great promise for its real field application to effectively monitor and control CBCVd infection in hop plants.

4. Conclusions

A sensitive and label-free genosensor for the impedimetric detection of CBCVd with good selectivity was developed. The architecture of the genosensor involves non-covalent immobilization of a biotinylated single-stranded DNA capture probe on the supporting GCE modified with a layer of streptavidin-agarose beads with incorporated 2D $Ti_3C_2T_x$ MXene electrocatalytic material. The 2D-layered $Ti_3C_2T_x$ was obtained by etching the Al layer of Ti_3AlC_2 by the HF method, with EDX spectra indicating a significant reduction of Al at% and high levels of F at%. Furthermore, XRD results indicated shifts in (002) and (004) peaks to lower 2θ values, caused by removing the Al layers in the initial structure of the MAX phase and induction of new surface terminations in $Ti_3C_2T_x$. After optimizing the fabrication and operational parameters, the synergy of the electrocatalytic MXene with other building blocks of the genosensor resulted in a low limit of detection of only 0.5 fg μL^{-1}, positioning this genosensor as a serious candidate for its on-site applications to monitor occurrence and progression of CBCVd directly in hop fields.

CRediT authorship contribution statement

Alnilan Lobato: Writing – original draft, Visualization, Methodology, Investigation, Formal analysis, Data curation, Conceptualization. **Ivan Konjević:** Visualization, Investigation, Formal analysis. **Sebastjan Radišek:** Supervision, Investigation, Funding acquisition, Formal analysis, Data curation. **Jernej Jakše:** Supervision, Investigation, Funding acquisition, Formal analysis. **Helena Volk:** Methodology, Investigation, Formal analysis, Data curation. **Monika Hermanová:** Methodology, Formal analysis. **Miroslav Fojta:** Supervision, Methodology, Funding acquisition, Formal analysis. **Jan Paštika:** Investigation, Formal analysis, Data curation. **Zdeněk Sofer:** Methodology, Investigation, Funding acquisition. **Rui Gusmão:** Writing – review & editing, Methodology, Investigation, Formal analysis, Data curation. **Samo B. Hočevar:** Writing – review & editing, Writing – original draft, Supervision, Funding acquisition. **Nikola Tasić:** Writing – review & editing, Writing

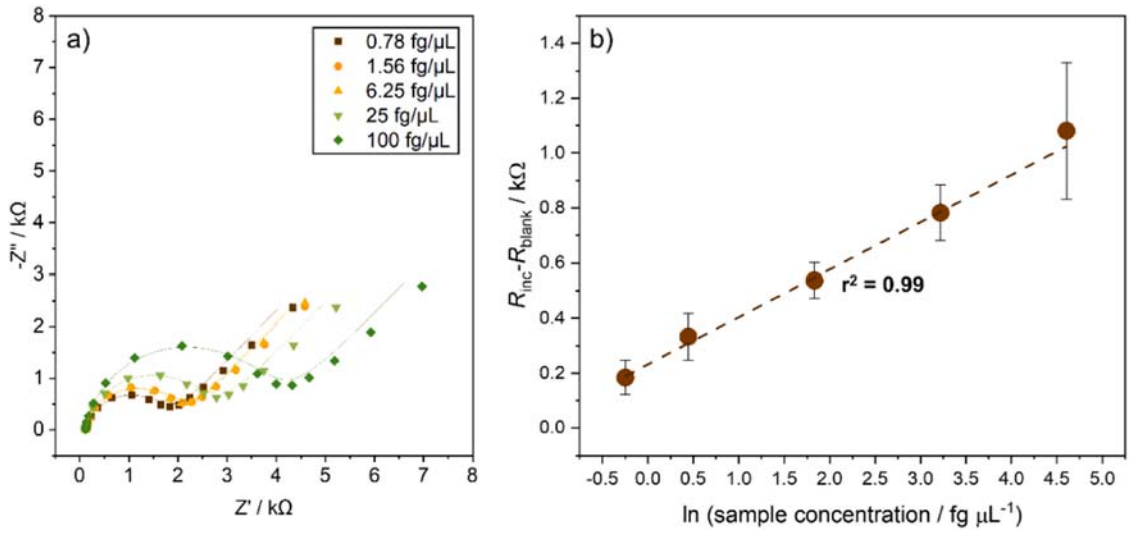

Fig. 5. (a) EIS spectra for increasing concentrations of CBCVd in real total RNA hop samples, and (b) corresponding calibration curve. The error bars represent the relative standard deviation of three independent measurements.

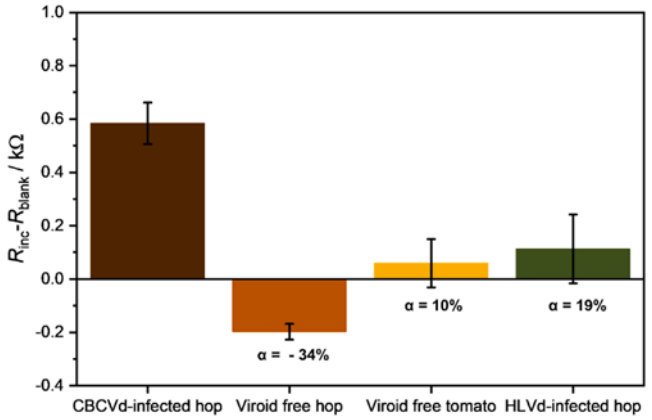

Fig. 6. Response of the genosensor in real total RNA samples containing interferents with corresponding selectivity factor values (α) calculated by dividing the analytical signal of an individual interferent by the analytical signal of the infected total RNA hop sample.

– original draft, Visualization, Supervision, Methodology, Formal analysis, Data curation.

Declaration of Competing Interest

The authors declare that they have no known competing financial interests or personal relationships that could have appeared to influence the work reported in this paper.

Acknowledgments

This research received funding from the Slovenian Research Agency: Research Program P1–0034, Program P4–0077, Research Project J1–3017, the Slovenian Research Agency's Young Researchers Program - grant agreement No. 56119, and the Czech Science Foundation project 21–46325L. The project was co-financed by the Republic of Slovenia, the Ministry of Education, Science and Sport, and the European Union under the European Regional Development Fund. Z.S. was supported by ERC-CZ program (project LL2101) from Ministry of Education Youth and Sports (MEYS) and AMULET project from Programme Johannes Amos Comenius, co-funded by EU (CZ.02.01.01/00/22_008/0004558). This work was in part supported from the grant of UCT Prague specific university research – grant No A2_FCHT_2024_076.

Appendix A. Supporting information

Supplementary data associated with this article can be found in the online version at doi:10.1016/j.snb.2024.136762.

Data Availability

Data will be made available on request. Characterization datasets generated and/or analyzed during the study are accessible via the Zenodo repository: 10.5281/zenodo.13889765.

References

[1] C. Almaguer, C. Schönberger, M. Gastl, E.K. Arendt, T. Becker, Humulus lupulus - a story that begs to be told. A review, J. Inst. Brew. 120 (2014) 289–314, https://doi.org/10.1002/jib.160.
[2] M. Karabín, T. Hudcová, L. Jelínek, P. Dostálek, Biologically active compounds from hops and prospects for their use, Compr. Rev. Food Sci. Food Saf. 15 (2016) 542–567, https://doi.org/10.1111/1541-4337.12201.
[3] J. Kubeš, Geography of world hop production 1990–2019, J. Am. Soc. Brew. Chem. 80 (2022) 84–91, https://doi.org/10.1080/03610470.2021.1880754.
[4] T.O. Diener, Viroids and the nature of viroid diseases*, in: 100 Years of Virology, Springer Vienna, Vienna, 1999, pp. 203–220, https://doi.org/10.1007/978-3-7091-6425-9_15.
[5] R. Flores, S. Minoia, A. Carbonell, A. Gisel, S. Delgado, A. López-Carrasco, B. Navarro, F. Di Serio, Viroids, the simplest RNA replicons: how they manipulate their hosts for being propagated and how their hosts react for containing the infection, Virus Res. 209 (2015) 136–145, https://doi.org/10.1016/J.VIRUSRES.2015.02.027.
[6] A. Hadidi, L. Sun, J.W. Randles, Modes of viroid transmission, Cells 11 (2022), https://doi.org/10.3390/cells11040719.
[7] N. Duran-Vila, C.N. Roistacher, R. Rivera-Bustamante, J.S. Semancik, A definition of citrus viroid groups and their relationship to the exocortis disease, J. Gen. Virol. 69 (1988) 3069–3080, https://doi.org/10.1099/0022-1317-69-12-3069.
[8] H. Puchta, K. Ramm, R. Luckinger, R. Hadas, M. Bar-Joseph, H.L. Saänger, Primary and secondary structure of citrus viroid IV (CVd IV), a new chimeric viroid present in dwarfed grapefruit in Israel, Nucleic Acids Res. 19 (1991), https://doi.org/10.1093/nar/19.23.6640.
[9] J. Jakse, S. Radisek, T. Pokorn, J. Matousek, B. Javornik, Deep-sequencing revealed Citrus bark cracking viroid (CBCVd) as a highly aggressive pathogen on hop, Plant Pathol. 64 (2015) 831–842, https://doi.org/10.1111/PPA.12325.
[10] EPPO, Citrus Bark Cracking Viroid, EPPO datasheets on pests recommended for regulation, ⟨Https://Gd.Eppo.Int/Taxon/CBCVD0/Datasheet⟩ (2024).
[11] M. Eiras, A.M. de Oliveira, A. de Fátima Ramos, R. Harakava, J.-A. Daròs, First report of citrus bark cracking viroid and hop latent viroid infecting hop in commercial yards in Brazil, 603–603, J. Plant Pathol. 105 (2023), https://doi.org/10.1007/s42161-023-01313-4.
[12] P. Baldi, N. La Porta, Molecular approaches for low-cost point-of-care pathogen detection in agriculture and forestry, Front. Plant Sci. 11 (2020) 1603, https://doi.org/10.3389/FPLS.2020.570862/BIBTEX.

[13] F. Martinelli, R. Scalenghe, S. Davino, S. Panno, G. Scuderi, P. Ruisi, P. Villa, D. Stroppiana, M. Boschetti, L.R. Goulart, C.E. Davis, A.M. Dandekar, Advanced methods of plant disease detection. A review, Agron. Sustain Dev. 35 (2015) 1–25, https://doi.org/10.1007/s13593-014-0246-1.
[14] Z. Zhang, S. Li, Detection of Viroids, in: Fundamentals of Viroid Biology, Elsevier, 2024, pp. 297–321, https://doi.org/10.1016/B978-0-323-99688-4.00017-1.
[15] A. Mokhtarzadeh, R. Eivazzadeh-Keihan, P. Pashazadeh, M. Hejazi, N. Gharaatifar, M. Hasanzadeh, B. Baradaran, M. de la Guardia, Nanomaterial-based biosensors for detection of pathogenic virus, TrAC Trends Anal. Chem. 97 (2017) 445–457, https://doi.org/10.1016/J.TRAC.2017.10.005.
[16] E. Cesewski, B.N. Johnson, Electrochemical biosensors for pathogen detection, Biosens. Bioelectron. 159 (2020) 112214, https://doi.org/10.1016/J.BIOS.2020.112214.
[17] S.S. Low, H.S. Loh, J.S. Boey, P.S. Khiew, W.S. Chiu, M.T.T. Tan, Sensitivity enhancement of graphene/zinc oxide nanocomposite-based electrochemical impedance genosensor for single stranded RNA detection, Biosens. Bioelectron. 94 (2017) 365–373, https://doi.org/10.1016/J.BIOS.2017.02.038.
[18] Y. Wang, W. Wang, X. Lu, T. Chen, Y. Wang, Y. Wen, J. Hu, J. Song, X. Wang, Novel RNA genosensor based on highly stable gold nanoparticles decorated phosphorene nanohybrid with graphene for highly sensitive and low-cost electrochemical detection of coconut cadang-cadang viroid, Microchim. Acta 191 (2024), https://doi.org/10.1007/s00604-023-06130-1.
[19] N. Štajner, S. Radišek, A.K. Mishra, V.S. Nath, J. Matoušek, J. Jakše, Evaluation of disease severity and global transcriptome response induced by Citrus bark cracking viroid, Hop latent viroid, and their co-infection in hop (Humulus lupulus L.), Int. J. Mol. Sci. 20 (2019), https://doi.org/10.3390/ijms20133154.
[20] B. Kump, B. Javornik, Evaluation of genetic variability among common buckwheat (Fagopyrum esculentum Moench) populations by RAPD markers, Plant Sci. 114 (1996) 149–158, https://doi.org/10.1016/0168-9452(95)04321-7.
[21] A. Sečnik, S. Radišek, N. Štajner, J. Jakše, Studying strands polarity of different viroids and their combinations in infected hop plants, Acta Agric. Slov. 115 (2020) 193–201, https://doi.org/10.14720/AAS.2020.115.1.1319.
[22] J. Isailović, A. Oberlintner, U. Novak, M. Finšgar, F.M. Oliveira, J. Paštika, Z. Sofer, N. Tasić, R. Gusmão, S.B. Hočevar, Study of chitosan-stabilized $Ti_3C_2T_x$ MXene for ultrasensitive and interference-free detection of gaseous H_2O_2, ACS Appl. Mater. Interfaces 15 (2023) 31643–31651, https://doi.org/10.1021/acsami.3c05314.
[23] T. Parker, D. Zhang, D. Bugallo, K. Shevchuk, M. Downes, G. Valurouthu, A. Inman, B. Chacon, T. Zhang, C.E. Shuck, Y.J. Hu, Y. Gogotsi, Fourier-transform infrared spectral library of MXenes, Chem. Mater. 17 (2024) 8437–8446, https://doi.org/10.1021/acs.chemmater.4c01536.
[24] X. Meng, D. O'Hare, S. Ladame, Surface immobilization strategies for the development of electrochemical nucleic acid sensors, Biosens. Bioelectron. (2023) 115440, https://doi.org/10.1016/j.bios.2023.115440.
[25] A. Holmberg, A. Blomstergren, O. Nord, M. Lukacs, J. Lundeberg, M. Uhlén, The biotin-streptavidin interaction can be reversibly broken using water at elevated temperatures, Electrophoresis 26 (2005) 501–510, https://doi.org/10.1002/elps.200410070.
[26] J. Tse, Y. Wang, T. Zengeya, E. Rozners, A. Tan-Wilson, Peptide nucleic acid probe for protein affinity purification based on biotin–streptavidin interaction and peptide nucleic acid strand hybridization, Anal. Biochem 470 (2015) 34–40, https://doi.org/10.1016/j.ab.2014.10.005.
[27] Q. Guo, J.-J. Han, S. Shan, D.-F. Liu, S.-S. Wu, Y.-H. Xiong, W.-H. Lai, DNA-based hybridization chain reaction and biotin–streptavidin signal amplification for sensitive detection of Escherichia coli O157:H7 through ELISA, Biosens. Bioelectron. 86 (2016) 990–995, https://doi.org/10.1016/j.bios.2016.07.049.
[28] H. Yin, H. Wang, W. Jiang, Y. Zhou, S. Ai, Electrochemical immunosensor for N6-methyladenosine detection in human cell lines based on biotin-streptavidin system and silver-SiO_2 signal amplification, Biosens. Bioelectron. 90 (2017) 494–500, https://doi.org/10.1016/j.bios.2016.10.066.
[29] C. Ling, L. Shi, Y. Ouyang, J. Wang, Searching for highly active catalysts for hydrogen evolution reaction based on O-terminated MXenes through a simple descriptor, Chem. Mater. 28 (2016) 9026–9032, https://doi.org/10.1021/acs.chemmater.6b03972.
[30] X. An, W. Wang, J. Wang, H. Duan, J. Shi, X. Yu, The synergetic effects of Ti_3C_2 MXene and Pt as co-catalysts for highly efficient photocatalytic hydrogen evolution over g-C_3N_4, Phys. Chem. Chem. Phys. 20 (2018) 11405–11411, https://doi.org/10.1039/C8CP01123K.
[31] Y. Xie, Y. Dall'Agnese, M. Naguib, Y. Gogotsi, M.W. Barsoum, H.L. Zhuang, P.R. C. Kent, Prediction and characterization of MXene nanosheet anodes for non-lithium-ion batteries, ACS Nano 8 (2014) 9606–9615, https://doi.org/10.1021/nn503921j.
[32] M. Naguib, J. Halim, J. Lu, K.M. Cook, L. Hultman, Y. Gogotsi, M.W. Barsoum, New two-dimensional Niobium and vanadium carbides as promising materials for Li-Ion batteries, J. Am. Chem. Soc. 135 (2013) 15966–15969, https://doi.org/10.1021/ja405735d.
[33] A. Junkaew, R. Arróyave, Enhancement of the selectivity of MXenes (M_2C, M = Ti, V, Nb, Mo) *via* oxygen-functionalization: promising materials for gas-sensing and -separation, Phys. Chem. Chem. Phys. 20 (2018) 6073–6082, https://doi.org/10.1039/C7CP08622A.
[34] M. Lian, Y. Shi, L. Chen, Y. Qin, W. Zhang, J. Zhao, D. Chen, Cell membrane and V_2C MXene-based electrochemical immunosensor with enhanced antifouling capability for detection of CD44, ACS Sens. (2022), https://doi.org/10.1021/acssensors.2c01215.
[35] H. Wang, J. Sun, L. Lu, X. Yang, J. Xia, F. Zhang, Z. Wang, Competitive electrochemical aptasensor based on a cDNA-ferrocene/MXene probe for detection of breast cancer marker Mucin1, Anal. Chim. Acta 1094 (2020) 18–25, https://doi.org/10.1016/j.aca.2019.10.003.
[36] A. Sinha, Dhanjai, H. Zhao, Y. Huang, X. Lu, J. Chen, R. Jain, MXene: an emerging material for sensing and biosensing, TrAC Trends Anal. Chem. 105 (2018) 424–435, https://doi.org/10.1016/j.trac.2018.05.021.
[37] A.A. Emerenciano, R.M. do Nascimento, A.P.C. Barbosa, K. Ran, W.A. Meulenberg, J. Gonzalez-Julian, Ti_3C_2 MXene membranes for gas separation: influence of heat treatment conditions on D-spacing and surface functionalization, Membrane 12 (2022) 1025, https://doi.org/10.3390/membranes12101025.
[38] T. Hu, M. Hu, B. Gao, W. Li, X. Wang, Screening surface structure of MXenes by high-throughput computation and vibrational spectroscopic confirmation, J. Phys. Chem. C 122 (2018) 18501–18509, https://doi.org/10.1021/acs.jpcc.8b04427.
[39] A. Sarycheva, Y. Gogotsi, Raman spectroscopy analysis of the structure and surface chemistry of $Ti_3C_2T_x$ MXene, Chem. Mater. 32 (2020) 3480–3488, https://doi.org/10.1021/acs.chemmater.0c00359.
[40] J. Azadmanjiri, J. Regner, L. Děkanovský, B. Wu, J. Luxa, Z. Sofer, Powering the future: unleashing the potential of MXene-based dual-functional photoactive cathodes in photo-rechargeable zinc-ion capacitor, Small (2023) 2305972, https://doi.org/10.1002/smll.202305972.
[41] L. Chaput, G. Hug, P. Pecheur, H. Scherrer, Thermopower of the 312 MAX phases Ti_3SiC_2, Ti_3GeC_2, and Ti_3AlC_2, Phys. Rev. B Condens Matter Mater. Phys. 75 (2007) 035107, https://doi.org/10.1103/PhysRevB.75.035107.
[42] M. Alhabeb, K. Maleski, B. Anasori, P. Lelyukh, L. Clark, S. Sin, Y. Gogotsi, Guidelines for synthesis and processing of two-dimensional titanium carbide ($Ti_3C_2T_x$ MXene), Chem. Mater. 29 (2017) 7633–7644, https://doi.org/10.1021/acs.chemmater.7b02847.

Alnilan Lobato is a Ph.D. student of Sensor Technologies at the International Postgraduate School Jožef Stefan and a young researcher at the Department of Analytical Chemistry, National Institute of Chemistry, Ljubljana, Slovenia. She obtained her MSc from the Chemistry Institute of the University of São Paulo (USP) in 2021 and her BSc in Bio-processes Engineering and Biotechnology from the State University of Rio Grande do Sul (UERGS) in 2019. Her research interests include electrochemical sensors and genosensors, and molecularly imprinted polymers.

Ivan Konjević is a Ph.D. student at the Faculty of Chemistry and Chemical Technology, University of Ljubljana. He obtained his MSc in Chemistry from the University of Maribor, Slovenia, in 2023, and BSc in Quality Control and Environmental Protection from the University of Sarajevo, Bosnia&Herzegovina, in 2019. His research interests include electrochemical sensors and genosensors, and application of electrochemistry for the atmospheric studies.

Sebastjan Radišek received his Ph.D. in 2004 at the University of Ljubljana, Biotechnical Faculty. Currently, he is the Head of the Plant Protection Laboratory, at the Slovenian Institute for Hop Research and Brewing, Žalec, Slovenia. His research interests include molecular markers, plant breeding, plant biotechnology, and phytopathology. He published more than 70 articles, with over 850 citations, with an h-index of 17.

Jernej Jakše received his Ph.D. in 2003 at the University of Ljubljana, Biotechnical Faculty. He is a Full Professor at the same faculty, and his research interests include plant genetics, molecular markers, DNA sequencing, next generation sequencing, and bioinformatics. He published more than 130 articles, with over 3500 citations, with an h-index of 34.

Helena Volk received her Ph.D. in 2019 at the University of Ljubljana, Biotechnical Faculty, Department of Agronomy. She currently works as a Teaching Assistant at the same faculty. Her research interests include genetics, biotechnology, statistics, and plant breeding.

Monika Hermanová received her Ph.D. in 2018 at the Masaryk University, Faculty of Science, Department of Experimental Biology. She currently works at the Department of Biophysical Chemistry and Molecular Oncology, Institute of Biophysics ASCR. Her research encompasses the fields of electrochemistry, biochemistry and analytical chemistry.

Miroslav Fojta studied biochemistry at the Charles University in Prague and earned his PhD (1995) in biophysics at IBP CAS, with Prof. E. Paleček. In 2005, he became the head of the DBCMO and finished his habilitation at the Masaryk University in Brno, where he was a group leader at the Central European Institute of Technology in 2011–2020. His research interests include electrochemistry of nucleic acids, chemical modification of biopolymers, and its application in the analysis of nucleotide sequences, DNA damage, and protein-DNA interactions.

Jan Paštika is a Ph.D. student at the Department of Inorganic Chemistry at the University of Chemistry and Technology in Prague, Czech Republic. He has published nine articles in peer reviewed journals, and his research interests include the synthesis and characterization of 2D layered materials.

Zdeněk Sofer has been a Full Professor at the University of Chemistry and Technology in Prague, Czech Republic, since 2018. He also received his Ph.D. from the University of Chemistry and Technology in Prague in 2008. During his Ph.D., he spent one year at Forschungszentrum Julich (Peter Grünberg Institute, Germany), followed by postdoctoral

experience in Germany. He is an Associated Editor of FlatChem journal. He has published more than 600 articles, which received almost 30,000 citations (h-index 88). His research interests include the synthesis of semiconductors and 2D materials, chemical modifications, and electrochemistry.

Rui Gusmão obtained his Ph.D. in Chemistry from the University of Barcelona, Spain, in 2012. As a postdoctoral researcher, he worked in Portugal at the University of Porto (2012–2013) and the University of Minho (2013–2016), followed by a position at Nanyang Technological University, Singapore (2016–2017). Since 2018, he has been a senior scientist at the Department of Inorganic Chemistry of the University of Chemistry and Technology in Prague, Czech Republic. In 2020 he received financial support under the GAČR Jr program. He has published over 50 articles in peer-reviewed journals and has an h-index of 23. His current research interests include the electrochemical applications of 2D layered materials.

Samo B. Hočevar received a Ph.D. in Analytical Chemistry in 2002 from the Faculty of Chemistry and Chemical Technology, University of Ljubljana, Ljubljana, Slovenia. Presently, he is the Head of the Department of Analytical Chemistry at the National Institute of Chemistry. His research interests include the development, study, miniaturization, and application of advanced electrochemical sensors, gas sensors, and biosensors.

Nikola Tasić is a Research Assistant Professor at the Department of Analytical Chemistry, National Institute of Chemistry, Ljubljana, Slovenia. He received both a MSc in Biochemical Engineering and Biotechnology and a Ph.D. in Materials Science and Engineering from the Faculty of Technology and Metallurgy, University of Belgrade, Belgrade, Serbia. He worked as a post-doctoral researcher at the Chemistry Institute, University of São Paulo, São Paulo, Brazil. His current research topics include the design and optimization of new methodologies applicable in point-of-need electrochemical biosensing, genosensing, immunosensing, and gas sensing.